

# Prediction of Viscous Forces on Oscillating Cylinders by Reynolds-Averaged Navier-Stokes Solver

Richard Korpus<sup>a</sup>, Paul Jones<sup>a</sup>, Owen Oakley<sup>b</sup>, and Leonard Imas<sup>c</sup>

<sup>a</sup> Science Applications International Corporation, Annapolis, Maryland USA

<sup>b</sup> Chevron Petroleum Technology Company, San Ramon, California USA

<sup>c</sup> University of Minnesota, Dept. of Aerospace Engineering, Minneapolis, Minnesota USA

## ABSTRACT

An unsteady, three-dimensional, overset-grid, Reynolds-Averaged Navier-Stokes (RANS) method is applied to the problem of vortex shedding behind fixed and moving circular cylinders. The flows selected for study are of particular interest to the offshore industry in that they represent various modes of riser excitation and response. Three distinct sets of simulations are presented with the objective of validating the method: stationary cylinders; cylinders undergoing forced motion; and cylinders free to undergo Vortex-Induced Vibration (VIV). A limited number of high-resolution simulations are also presented to investigate the impact of small, spanwise phenomena such as "braid" vortices.

## INTRODUCTION

As offshore production moves towards deeper tracts, the potential for Vortex Induced Vibration (VIV) of risers becomes a greater concern. Lateral forces induced by vortices shed along the riser lead to a large amplitude hydro-elastic response. The associated increase in drag can be significant. Since VIV flows are complex, the analysis of fluid-induced riser motion has remained a somewhat empirical science. This limitation has not proven insurmountable for shallow-water riser analysis, but has become a problem for deep-water risers where empirical descriptions of hydrodynamic forces are insufficient for robust engineering analysis.

Reliable analysis of deep-water risers requires an approach that can supplement existing empirical knowledge. One potential approach is to utilize advanced computational techniques to provide first-principals fluid forcing. The objective of the work presented herein is to investigate the applicability of state-of-the-art Computational Fluid Dynamics (CFD) tools for predicting VIV forces; and to validate this applicability against experimental data.

Since VIV is a vortex-driven fluid/structures coupling phenomena, any computational approach to its solution must resolve unsteady, moving-body, three-dimensional, viscous flows at (potentially) high Reynolds numbers. A truly robust modeling of the problem therefore requires numerical techniques capable of capturing (at least) the creation of vorticity in the boundary layer, the shedding of vorticity at separation, and the effects of turbulence on pressure in the wake. One set of CFD tools for resolving these flows is the group known as Reynolds-Averaged Navier-Stokes (RANS) solvers. The advantages of RANS for offshore applications have already been well demonstrated

by Yeung and Vaidhyanathan (1993), Schulz and Kallinderis (1997), and others.

This paper describes the application and validation of an incompressible, time-accurate, overset-grid RANS method for the analysis of deep-water riser dynamics problems. Body motions are either prescribed using a predetermined function of time (forced-motion), or by integrating the riser equations of motion as the solution progresses (free-vibration response due to vortex-induced excitations). Three distinct physical regimes have been investigated: stationary cylinders with oscillatory wakes; cylinders undergoing forced motion; and freely-vibrating cylinders undergoing vortex-induced excitation. Because the number of calculations required to characterize a riser's response in any one of these classes is large, most of simulations were performed using poor resolution grids along the axis of the riser. A fourth set of simulations is therefore included to investigate the effect of small-scale, three-dimensional effects using higher resolution grids.

## APPROACH

The time-dependent viscous flow solutions presented in this study were obtained by solving the incompressible RANS equations in conjunction with a  $k\varepsilon$  turbulence model. When non-dimensionalized by a characteristic length  $L$ , velocity  $V_0$ , and density  $\rho$ , the Cartesian form of these governing equations can be written

$$\nabla \cdot \mathbf{V} = 0 \quad (1)$$

$$\frac{\partial \mathbf{V}}{\partial t} + \mathbf{V} \cdot \nabla \mathbf{V} + \nabla p - \frac{1}{\text{Re}} \nabla^2 \mathbf{V} - \nabla \cdot \boldsymbol{\tau} = \mathbf{F} \quad (2)$$

$$\frac{\partial k}{\partial t} + \mathbf{V} \cdot \nabla k - \left( \frac{1}{\text{Re}} + v_t \right) \nabla^2 k - P + \varepsilon = 0 \quad (3)$$

$$\begin{aligned} \frac{\partial \varepsilon}{\partial t} + \mathbf{V} \cdot \nabla \varepsilon - \left( \frac{1}{\text{Re}} + \frac{v_t}{1.3} \right) \nabla^2 \varepsilon - \frac{\varepsilon}{k} (c_{\varepsilon 1} P_{sol} + c_{\varepsilon 3} P_{irr}) \\ + c_{\varepsilon 2} \frac{\varepsilon^2}{k} = 0 \end{aligned} \quad (4)$$

where the Reynolds stress components  $\tau_{ij}$  are defined by the Boussinesq approximation,

$$\tau_{ij} \equiv -\frac{2}{3} k \delta_{ij} + v_t S_{ij}, \quad S_{ij} = \frac{\partial u(i)}{\partial x^j} + \frac{\partial u(j)}{\partial x^i} \quad (5)$$

and  $[x^1, x^2, x^3]^T$  represents the Cartesian position vector.  $\mathbf{V}$  represents

the Cartesian velocity's vector  $[u(1),u(2),u(3)]^T$ ,  $p$  the pressure,  $k$  the turbulent kinetic energy, and  $\varepsilon$  the turbulent dissipation rate.  $\mathbf{F}$  is an arbitrary body force, and can be used to represent hydrostatic pressure when free surface effects are important. The quantity  $\nu_t$  is defined as the linear eddy viscosity  $.09 k^2/\varepsilon$ , and  $Re$  the Reynolds number  $LV_0/\nu$ . The modeling coefficients  $C_{\varepsilon 1}$ ,  $C_{\varepsilon 2}$ ,  $C_{\varepsilon 3}$  are taken as constants equal to (1.44,1.92,2.4), respectively. Additional details of the turbulence model can be found in Chen and Patel (1988) and Hanjalic and Launder (1980). It should be noted that some of the reported simulations were repeated using a Baldwin-Lomax turbulence model, but that little effect was seen in the results.

Computations about complex geometries require that Equations (1) through (4) be first transformed into body fitted coordinates. Discretization is accomplished by linearizing the resulting equations over a single computational element, and solving analytically by separation of variables. Evaluation of the analytic solution at the interior node of a computational element provides a stencil for the center point in terms of its nearest neighbors. Time derivatives are handled by the Euler implicit method, and the algebraic system solved by the alternating direction implicit (ADI) method in each cross-flow plane. The approach is described in Chen and Korpus (1993) and Chen and Patel (1989). Detailed expressions for the difference stencil can be found in Chen et al. (1990).

Simulations around complex or moving geometries are accomplished by embedding the discrete forms of Eqs. (1) through (4) in a multi-block overset-grid environment. The solver works on one block at a time, and the only grid connectivity requirement is that the union of blocks spans the entire computational domain. Individual blocks are allowed to overlap arbitrarily, and inter-block communication is handled by conservative triquadratic interpolation. The overall approach has been extensively validated for both steady and unsteady three-dimensional applications in Korpus et. al. (1998), Korpus and Falzarano (1997), and Weems and Korpus (1994).

The overset advantage is demonstrated in Figure 1, which depicts a typical circular riser grid. The block containing the riser boundary layer can be resolved to any level without affecting the rest of the grid ( $y^+ \sim O(1)$  in this case). The boundary layer and wake blocks are set to move with the riser, whereas the intermediate and far field blocks remain Earth-fixed. Note that complications such as fairings or choke lines can be incorporated by simply adding blocks to represent them.

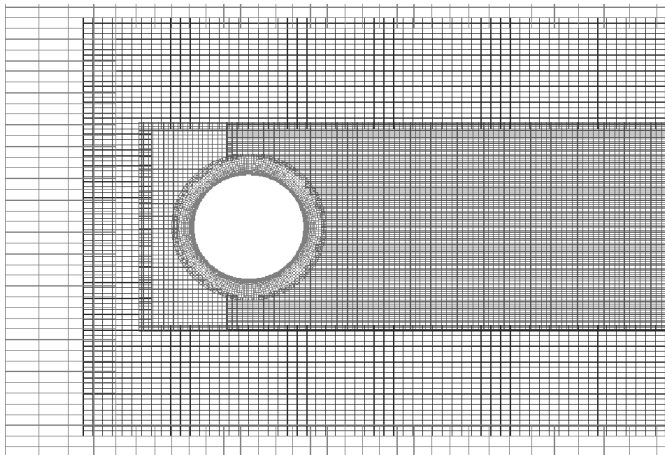


Figure 1: Overset Grid for Circular Cylinders

## STATIONARY CYLINDERS

A series of six simulations were performed for validating the ability of RANS to predict unsteady flows past stationary circular cylinders. The simulations represent regimes where risers will not respond due to

a disparity between forcing and structural frequencies. The six Reynolds numbers presented are:  $10^3$ ,  $10^4$ ,  $10^5$ ,  $8 \cdot 10^5$ ,  $2 \cdot 10^6$ , and  $10^7$ , which covers sub-, trans-, and supercritical flow regimes for separated flows around bluff bodies.

All six runs utilized three-dimensional grids with coarse resolution along the cylinder span. Most simulations used only five points from end to end, and little spanwise flow was therefore seen. While it is understood that shedding from three-dimensional cylinders creates an inherently three-dimensional flow, it was nonetheless decided to ignore these effects during the coarse calculations. Motivation for this decision is due solely to the need for limiting computer resources. A typical coarse grid calculation required only 75 Mbytes and 8 hours of CPU time on an SGI Octane.

Inflow boundary and the initial conditions are set to a uniform free stream flow. No-penetration "potential flow" walls are used for velocity boundary conditions on the top and bottom faces of the domain. Radiation boundary conditions are used at outflow (for all dependent variables), and for pressure (on all surfaces), to prevent reflections back into the domain. The radiation conditions work by computing a wave speed for each dependent variable that's unsteady at the boundary, and then assuming the wave travels one time step without distortion. Von Karman vortex streets form in all cases as a consequence of boundary layer separation, and no artificially-imposed perturbations on the mean flow are required.

Grid independence was achieved for this (and all) regimes by generating a series of geosym meshes. Successively finer grid spacing was used until mean and unsteady forces converged to within a few percent. The final grid is represented in Figure 1, uses an azimuthal resolution of 2 degrees. Wall-normal spacing on the body (non-dimensionalized by  $D$ ) is set to  $5 / Re$ , which is sufficient to place the first point at  $y^+ = 0.5$  for turbulent flow cases. The near wake block utilizes square cells of dimension  $0.02D$ , and extends a total of 4.5 diameters downstream from the cylinder center. The far-field block extends a total of 10 diameters upstream, 10 diameters above, 10 diameters below, and 20 diameters downstream from the cylinder. There are a total of 38000 points in each plane normal to the cylinder axis.

Since the RANS equations do not resolve the physics of boundary layer transition, the flow for each run was treated as either fully laminar or fully turbulent. Transition from laminar to turbulent is assumed to take place at a Reynolds number of 300,000 (based on diameter). While this simplification does not precisely simulate the behavior of turbulence statistics in the wake, it has proven adequate for force prediction since the largest contribution to force is whether the boundary layer separates at its laminar or turbulent location. This assumption may be less of a limitation for "real world" risers since transition is more gradual once roughness (or growth) is present.

Snapshots from one of the turbulent solutions (after steady shedding has set in) are shown in Figure 2. The upper portion shows contours of streamwise velocity, whereas the lower portion shows contours of spanwise vorticity. Development of the von Karman vortex street is clearly visible.

Figure 3 shows a time history of lift and drag force for the same case. The forces are seen to start symmetrically, with asymmetries growing until shedding becomes stationary (i.e. cyclic). Strouhal numbers for lift and drag are found to be 0.198 and 0.392, respectively. This is consistent with the experimentally observed Strouhal number

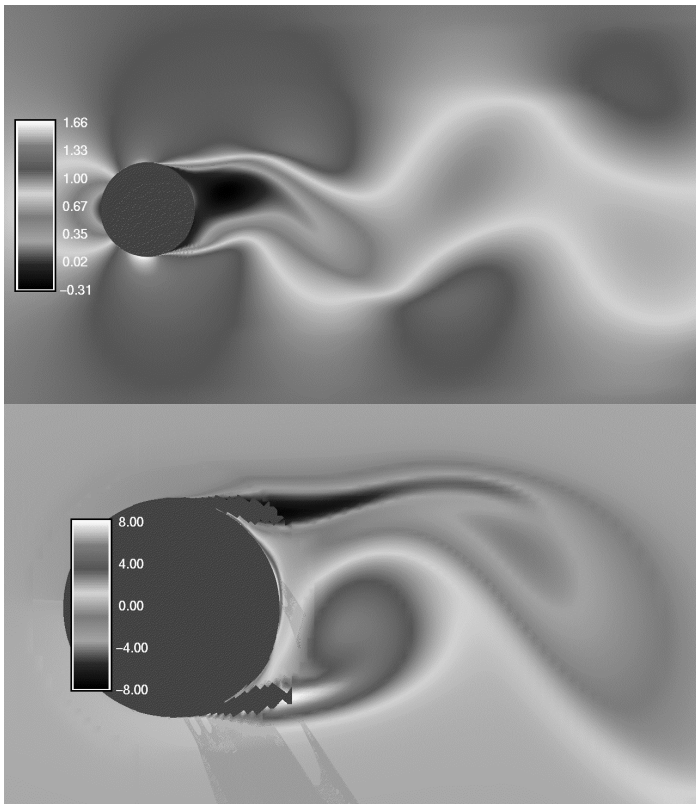


Figure 2: Typical High Reynolds Number Solution: Streamwise Velocity (Top), Spanwise Vorticity (Bot)

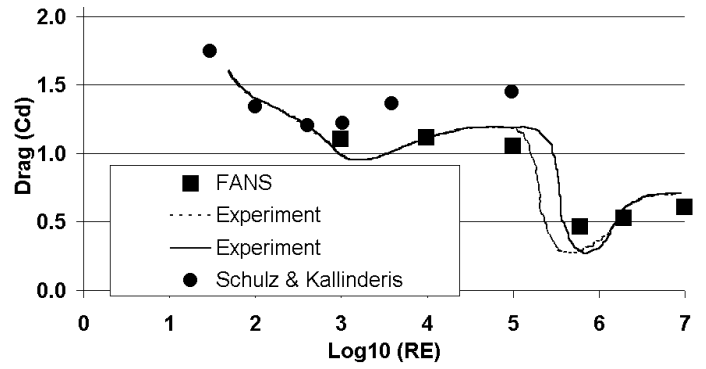


Figure 4: Drag Coefficient vs. Reynolds Number

(for lift) of between 0.16 and 0.19 for flows at sub-critical Reynolds numbers (Blevins, 1990). Figure 4 summarizes the computed mean drags for the six stationary cylinder runs (labeled RANS). Included for comparison are a similar set of RANS calculations by Schulz and Kallinderis (1997). Note that RANS simulations can not be expected to perform accurately in the transition region ( $10^5 < Re < 6 \cdot 10^5$ ) unless turbulent transition models are included.

### FORCED MOTIONS

Deep-sea risers exposed to sheared currents can undergo multi-modal or multi-frequency hydro-elastic response with standing or traveling structural wave propagation. While only a specific portion of the riser may lock-in during such an event, the resulting wave-like structural behavior will drive the excitation in the remainder of the structure. The investigation of forced motion is therefore important for understanding how hydrodynamic forces vary as a function of excitation frequency and amplitude.

Two sets of validation-quality forced-motion experiments were selected for comparison: Sarpkaya (1978); and Hover, Techet, and Triantafyllou (1998). Both experiments measured transverse forces on a cylinder forced to oscillate perpendicular to a uniform stream, and both were conducted at low sub-critical Reynolds numbers and moderate forcing amplitude. Setup for the RANS simulations was made to match the second set of tests (hereafter referred to as the "MIT" experiments), and utilized a Reynolds number of 3800 and forcing amplitude of  $A/D = 0.4$ . Sarpkaya's experiments used an  $A/D$  of 0.5, but showed only slight variations with small changes in amplitude. Forcing was limited to a single frequency per simulation (as were the experiments), and was prescribed using the form  $y = A \cos(\omega t)$ . Forcing frequencies were selected to match ranges covered during the experiments, and were specified using the non-dimensional "reduced velocity"  $V_r = 2\pi U_{REF} / (\omega D)$ . Values of 3.0, 3.5, 4.0, 4.25, 4.5, 4.75, 5.0, 5.5, 6.0, 6.5, 7.0, 7.5, 8.0 were tested -- with the clustering selected to resolve steep sections of the experimental data.

All other aspects of problem setup are identical to those used for the stationary cylinder cases. Only coarse spanwise grids were used, and all runs were started from a uniform freestream with the cylinder placed at its maximum displacement. Wake blocks were made sufficiently wide so as to capture the entire vortex street even when the cylinder reaches maximum displacement.

Force histories in the transverse (lift) direction from three of these runs are shown in Figure 5. The three histories depict two distinctly different response modes, with both frequency and amplitude varying between them. The lateral force at  $V_r = 4.0$ , for example, has a half-amplitude of approximately 2.5 whereas the lower frequency (higher  $V_r$ ) cases show amplitudes closer to 1.0. The higher force required at  $V_r = 4$  indicates that lock-in has not occurred because self-excited motions would require less energy. The force Strouhal number

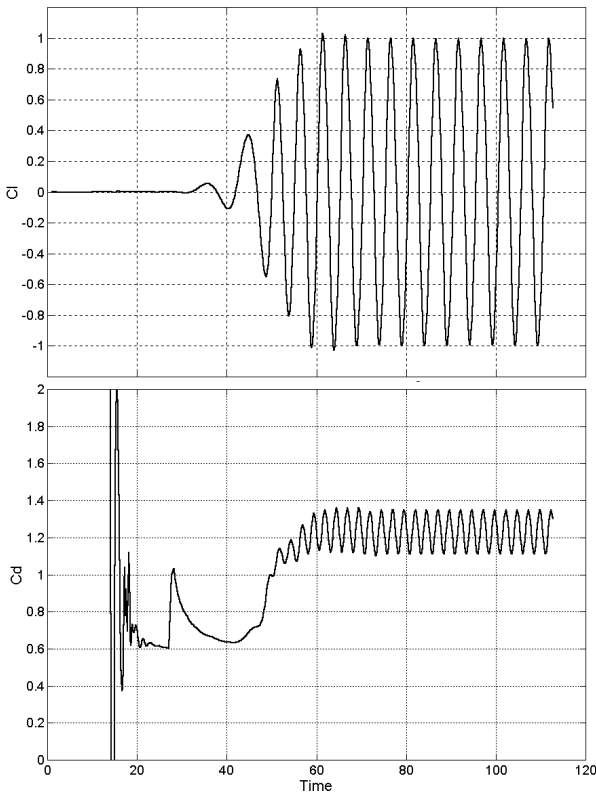


Figure 3: Cross-Flow Force (Top), In-Line (Bottom)

computed from the plot is 0.25, which also indicates lock-in at the Strouhal shedding frequency (approximately 0.2) has not occurred. The other two  $V_r$ 's both show force responses at  $St = 0.19$ , indicating that lock-in to the shedding frequency has taken place.

The in-line (drag) forces show many of the same trends as the lateral forces, and will not be shown here. Like the lateral force amplitude, mean drag is a fairly sensitive function of reduced velocity. At  $V_r = 4$  and  $V_r = 6$  the mean is around 1.5 or 1.6. At  $V_r = 8$  the mean is reduced to 1.2.

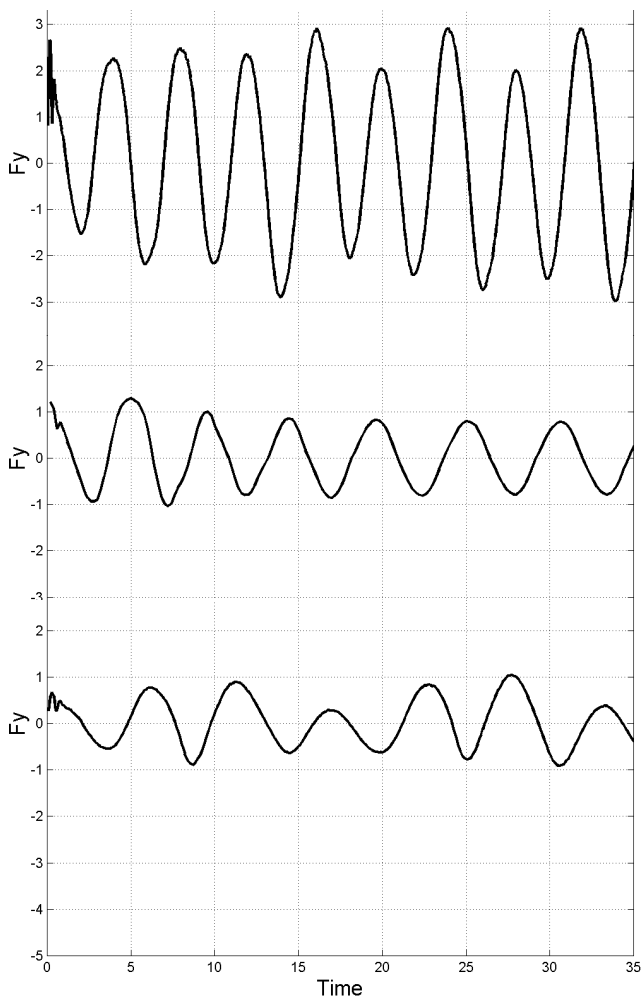


Figure 5: Lateral Force vs. Time –  $V_r=4$  (Top),  $V_r=6$  (Middle),  $V_r=8$  (Bottom)

Rather than present the large quantity of data represented by time histories and spectral decompositions (Fourier transforms) of response at each  $V_r$ , experimentalists typically report just the one Fourier component at the forcing frequency. While necessary due to space limitations, it is important to realize this approach may not tell the whole story. Many of the force histories exhibit multi-frequency response, but the results reported here give only the dominant response frequency. Computing force magnitudes at one frequency can also lead to variable results if the spectrum is particularly steep. Since all the spectra resulting from these simulations were effectively single- or multi-modal, this can be expected to be a major source of uncertainty in both the experimental and computational reporting.

With these caveats in mind, Figure 6 compares the RANS computed response at the forcing frequency to those obtained through experiments. Both MIT's and Sarpkaya's data are plotted, and the

Fourier transform magnitude is included along with real (CLA) and imaginary (CLV) component breakdowns. CLA is the lift in phase with acceleration, from which the added mass is computed; CLV is the lift in phase with velocity. The first conclusion available from these figures is that there is a significant difference between two experiments that were intended to be similar in setup

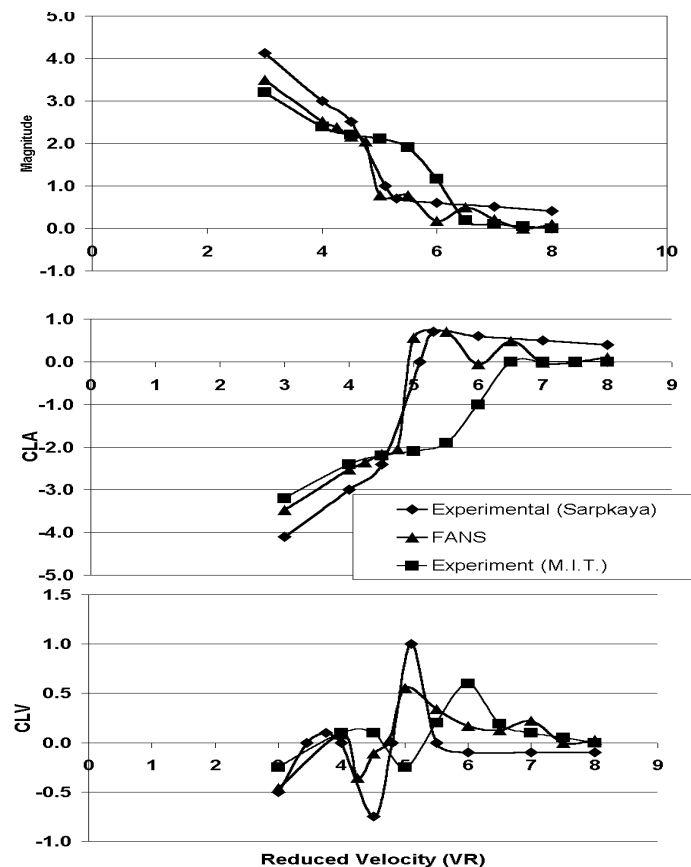


Figure 6: Forces at Motion Frequency – Magnitude (Top), CLA (Middle), and CLV (Bottom)

The RANS results compare fairly well to Sarpkaya's data through most of the  $V_r$  range, and capture the phase change and magnitude drop at  $V_r = 5$  quite accurately. While the comparison to CLA and magnitude are good, however, RANS resolves the CLV curve only qualitatively. Both peaks are under-predicted, and the sign is wrong at high  $V_r$ 's. Since CLV is a smaller quantity than CLA, the overall level of accuracy is not seriously affected, and remains within 20% of Sarpkaya's data. When compared to the MIT data RANS does not fare as well. Only at  $V_r$ 's below 5 and above 7 is the comparison favorable.

While it is difficult to say which experiment provides the best data for validation, there are certain qualitative indicators that might be used for guidance. In particular, the onset of lock-in should be accompanied by both a phase change (from following force to leading force), and a drop in total force magnitude (as less input energy is required to drive the cylinder). Since lock-in typically occurs between  $V_r = 5$  and  $V_r = 8$ , one would expect this phase change to occur around  $V_r = 5$ . Both Sarpkaya's data and the RANS results predict this change.

### SELF-INDUCED MOTIONS (VIV)

The third flow regime to be investigated is the class of Vortex-Induced Vibrations (VIV) problems. VIV occurs whenever fluid

forcing frequencies approach a natural structural mode, and can be expected to become more common as riser length increases.

Due to the interactive nature of VIV, solving these problems requires the simultaneous solution of fluid flow and structural response. The structural response part is treated herein as entirely two-dimensional. This is not a limitation for the current work since most validation data is presented in this form. More general engineering solutions, however, will require three-dimensional structural models to resolve allowable mode shapes.

The experiments of Hover, et. al. (1998) were selected for validation. The tests were performed by “driving” cylinders at the same displacement they would experience had they been spring mounted to undergo free vibrations. The prescribed motions are obtained by measuring the fluid excitation forces in real-time, integrating the equations of motion, and then forcing the cylinder mounts to move to the prescribed location. This is essentially the same approach used in the CFD simulations.

Setup for the CFD simulations is exactly the same as described in the forced-motion section, except that the cylinder is now initially positioned with zero displacement and velocity. The cylinder’s trajectory is computed as part of the solution process by integrating the equations of motion to move the grid at each time step. Two types of simulations were performed: one degree-of-freedom (1-DOF) and two degree-of-freedom (2-DOF). In either case, the equations of motion were defined using the same mass and damping ratios as the experiments, and varying the spring constant to give the desired natural structural frequency.

Since the original intent of this run series was validation, most of the simulations were performed like the experiments -- using only one degree-of-freedom. The series consisted of nine runs in total, at  $Vr$ ’s of 3.0, 4.5, 5.0, 5.5, 6.0, 6.5, 7.0, 7.5, and 8.0. Figure 7 plots the resulting forces versus a reduced velocity ( $Vr$ ) based on system natural frequency (obtained via Fourier transform of displacement), tow velocity, and cylinder diameter.

Both the magnitude and phase are shown, and the experimental data is included for comparison. The magnitudes are typically within 20% of their experimental values, and phase is predicted very well. The only significant difference is that the computations predict onset of “lock in” (phase reversal) at  $Vr=4.5$  whereas the experiments show  $Vr=5.5$ . This difference may be attributed due to RANS limitations in modeling transition. The Strouhal number (inverse of  $Vr$ ) corresponding to lock-in can shift between 0.16 and 0.22, depending on whether the flow is closer to the sub-critical end or the super-critical end of the transition regime (Blevins, 1990). Since RANS modeling requires that the Reynolds number corresponding to this shift be specified, differences between computed and measured reduced velocities corresponding to lock-in may arise.

A single 2-DOF calculation was made in order to provide comparisons between the experimental world (DOF-limited) and the real world (DOF-unlimited). Figure 8 compares the results with an identical 1-DOF case, and shows some significant differences. First and foremost is that the amplitude of lateral displacement increases dramatically when the second degree-of-freedom is added -- from 0.6D to 1.0D. Mean drag also increases significantly -- from 2.2 to 3.5. Both differences could have serious impact on deep-water riser design, and future experiments should be designed with this in mind.

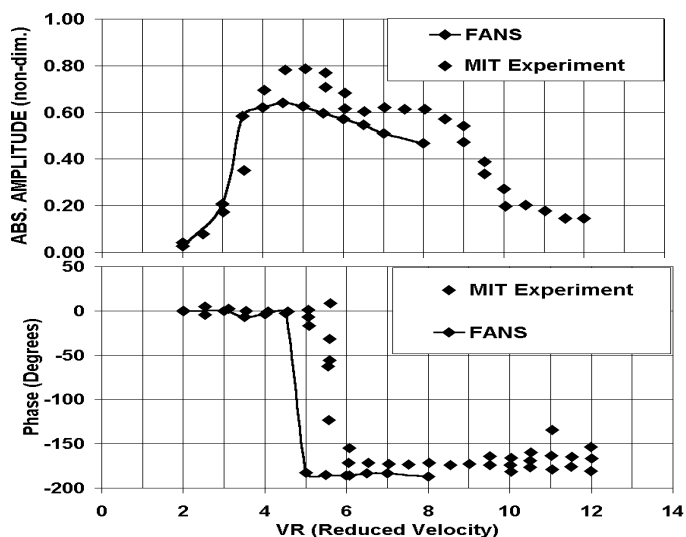


Figure 7: Lateral Displacement at System Natural Frequency -- Magnitude (Top); Phase (Bottom)

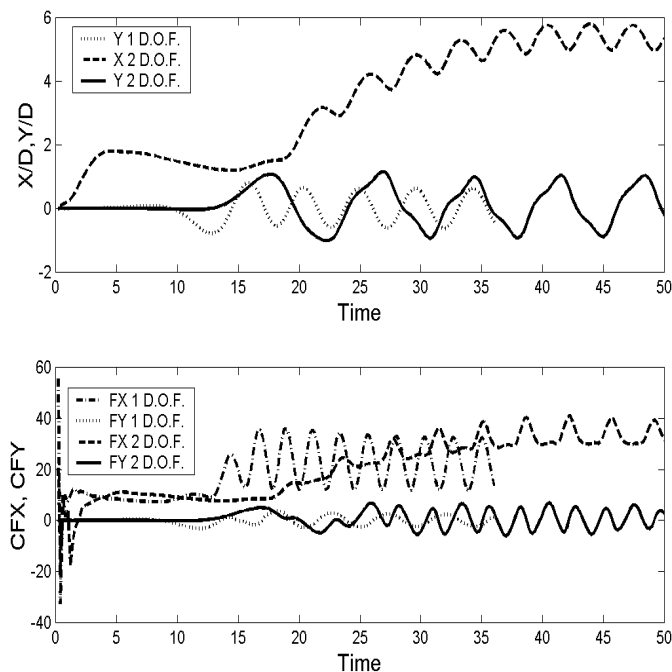


Figure 8: Comparison of 1-DOF and 2-DOF VIV

### THREE-DIMENSIONAL EFFECTS

Three-dimensional flows involving VIV contain physics that cause induced forces to vary along a cylinder’s span. Secondary instabilities in the von Karman vortex street, for example, result in “braid vortices” that are smaller than a cylinder diameter. It is important, therefore, to investigate how three-dimensional effects contribute to the hydrodynamic forces that drive riser excitation, and under what conditions two-dimensional flow assumptions can be considered valid.

This was accomplished using finer spanwise grids over a more limited portion of riser. The riser aspect ratio was chosen to be large enough so that three-dimensional span-wise flow coherence was not sensitive to variations in span, but short enough to permit grid resolution sufficient for resolving braid vortices. A new grid was built to span nine cylinder diameters using a uniform grid spacing of 0.1D.

Extrapolation boundary conditions were used at the cylinder ends to avoid prejudicing any cyclic behavior. The case of a stationary cylinder undergoing periodic shedding was chosen for these initial studies because of the large experimental data-base available on such flows. Two runs were completed: a sub-critical (laminar boundary layer) flow simulation at  $Re = 20,000$ , and a super-critical (turbulent flow) flow simulation at  $Re = 1,200,000$ .

Figure 9 depicts vorticity contours from the sub-critical Reynolds number result. The upper portion shows a longitudinal cut near the center of the cylinder, and demonstrates that the overall flow does not significantly differ from the coarse grid result of Figure 2. The lower portion, however, gives a cross-flow cut that depicts secondary instabilities growing on the shed shear layers. Figure 10 shows a surface of constant vorticity magnitude, and demonstrates that these instabilities eventually grow into streamwise “braid” vortices that connect successive von Karman vortices. The braids repeat approximately every three diameters, which compares well with Bearman’s (1984) observations that correlation length varies from  $3D$  at  $Re=10,000$  to  $6D$  at  $Re=100,000$ .

While the super-critical Reynolds number results (not shown) appear qualitatively similar, there are significant quantitative differences from the sub-critical case. The braid vortices of Figure 10 are not as well defined, and the strength of the braids is reduced. Braids in the sub-critical solution can be shown to have circulation magnitudes around 40% of that in the principal (spanwise) vortices. Braids in the super-critical case are only about 5% of principal.

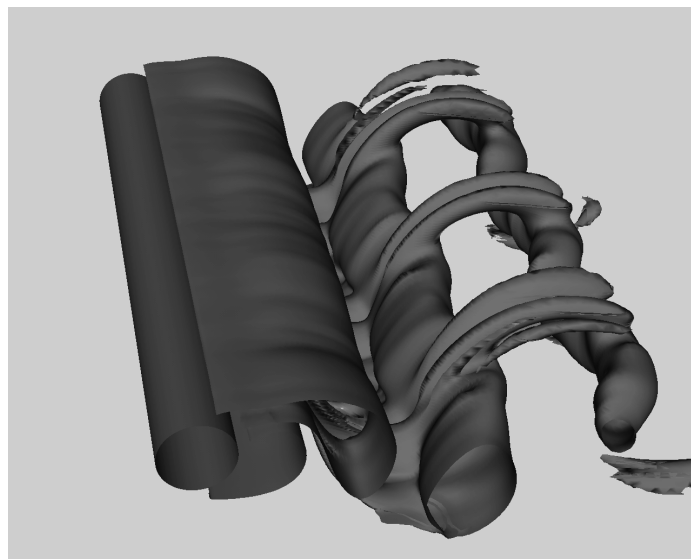


Figure 10: Surface of Constant Vorticity Magnitude

	Re = 20,000		Re = 1,200,000	
Grid	mean	amp.	mean	amp.
5x38000	0.0	0.95	0.0	0.44
90x38000	0.0	0.90	0.0	0.60

Table 1: Comparison of Lift Coefficients

	Re = 20,000		Re = 1,200,000	
Grid	mean	amp.	mean	amp.
5x38000	1.2	0.08	0.53	0.02
90x38000	1.2	0.12	0.67	0.07

Table 2: Comparison of Drag Coefficients

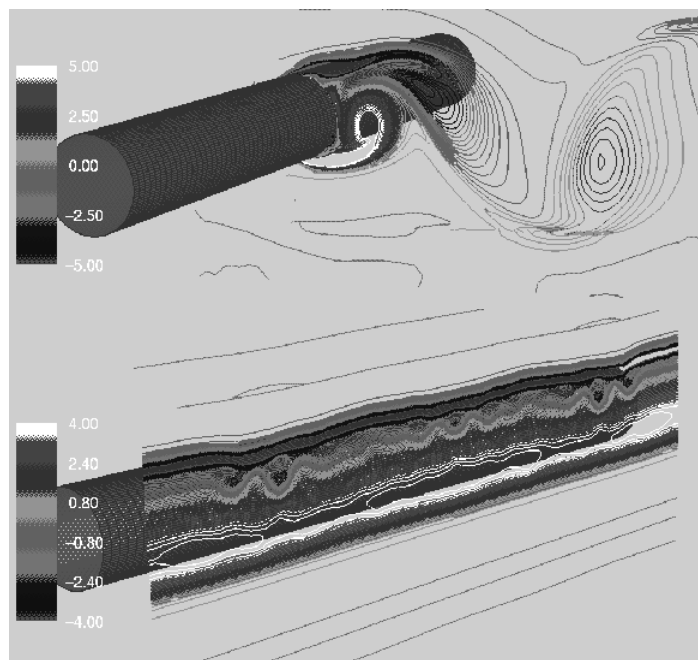


Figure 9: Vorticity Contours for  $Re = 20000$  – Spanwise (Top), Streamwise (Bottom)

The effect of three-dimensional flow on total force is summarized in Tables 1 and 2. The first column gives the number of grid points along the cylinder span and the number of points in each cross-flow plane. The first row represents the coarse grid results of Section 1. The remaining columns demonstrate that at sub-critical Reynolds numbers, computed drag is comparable between fine and coarse grid. At higher Reynolds numbers, however, both mean and unsteady drag components increase. Changes in lift are not as substantial, but still not trivial at the higher Reynolds number.

## CONCLUSIONS

The application of overset-grid, Reynolds-Averaged Navier-Stokes (RANS) solvers to the computation of VIV forces on bare cylinders has been a great success. Validation studies have indicated that unsteady forces can be computed accurately for three canonical problems of engineering relevance to the offshore industry: stationary cylinders with oscillatory wakes; cylinders forced to undergo prescribed motions; and cylinders experiencing Vortex-Induced Vibration (VIV).

The comparison of predicted to measured mean drag of stationary cylinders is within 10% or better at both sub and supercritical Reynolds numbers. Forced-motion simulations have also yielded quantitatively acceptable comparisons with available experimental data, but conclusions are more difficult to substantiate since the force measurements differ from experiment to experiment. RANS simulations accurately capture the onset of “lock-in” near  $V_r = 5$ , and predict corresponding force magnitudes to within 20% of (some) experimental data. Accuracy of predicted forces for freely oscillating cylinders is also within 20%, but with a slight over-prediction of the frequency at which VIV begins. The later being due to transition modeling limitations.

Three-dimensional, stationary cylinder studies have indicated that although description of key flow physics is missing from coarse (spanwise) grid calculations, the forces needed to support design studies do not necessarily require their resolution. RANS solutions do resolve the expected streamwise “braid” vortices, and show significant spanwise variations along the length of the cylinder, but forces at sub-critical Reynolds numbers show very little variation with the extra resolution.

Forces at super-critical Reynolds numbers, on the other hand, show more sensitivity to span-wise flow physics.

Finally, it should be noted that although both sub and supercritical flow regimes can be analyzed, transition between the two is an area where further research is required. The accurate calculation of forces near the critical Reynolds number has not been addressed herein, and will require the application of advanced transition models. For flows corresponding to sub- or supercritical Reynolds number regimes, the turbulence models employed herein have been shown valid for several VIV-related applications.

The validity of RANS-based CFD methods for unsteady, separated turbulent flows is discussed at length in Fertziger, et. al., (1999). The authors point out that although RANS methods do not model the physics of turbulence fluctuations, they do resolve the (mean) energy production and dissipation associated with unsteady turbulent flow. From a statistical stand-point, these flows are "stationary," and RANS methods should prove quite accurate (Imas, 1999). While this is still a debated subject, the validations presented herein demonstrate (at least partially) that RANS can reliably solve riser dynamics problems.

## REFERENCES

Bearman, P. W., 1984, "Vortex Shedding from Bluff Bodies," *Ann. Rev. Fluid Mech.*, vol. 16, pp 195.

Blevins, R. D., 1990, Flow-Induced Vibrations, Van Norstrand Reinhold, New York.

Chen, H.C., and Korpus, R.A., 1993, "A Multi-Block Finite-Analytic Reynolds-Averaged Navier-Stokes method for 3-D Incompressible Flows." *ASME J. of Fluids Engineering*.

Chen, H.C., and Patel, V.C., 1988, "Near-Wall Turbulence Models for Complex Flows Including Separation," *AIAA Journal*, Vol. 26, No. 4, pp. 641-648.

Chen, H.C., and Patel, V.C., 1989, "The Flow Around Wing-Body Junctions," *Proceedings, 4<sup>th</sup> Symposium on Num. And Phys. Aspects of Aerodynamic Flows*, Long Beach, CA.

Chen, H.C., Patel, V.C., and Ju, S., 1990, "Solutions of Reynolds-Averaged Navier-Stokes Equations for Three-Dimensional Incompressible Flows," *J. of Computational Physics*, Vol. 88, No.2, pp. 305-336.

Fertziger, J. H., and Milovan, P., 1999, Computational Methods for Fluid Dynamics, 2nd edition, Springer, New York.

Hanjalic, K., and Launder, B.E., 1980, "Sensitizing the Dissipation Equation to Irrotational Strains," *ASME J. of Fluids Engineering*, Vol. 102.

Hover, F., Techet, A., and Triantafyllou, M, 1998 "Forces on Oscillating Uniform and Tapered Cylinders in Cross Flow," *J. Fluid Mech.*, vol. 000, pp1-18.

Imas, Leonard, 1999, "Deep Star CTR4409 Report on Vortex-Induced Vibration," final report for BP-Amoco Stress Engineering Services, MARINTEK-USA.

Korpus, R., Hubbard, B., Jones, P., Stromgren, C., and Bennett, J., 1998, "Hydrodynamic Design of Integrated Propulsor/Stern Concepts by Reynolds-Averaged Navier-Stokes Technique," *Proc. of the 7<sup>th</sup> Int. Symp. On Practical Design of Ships and Mobile Units*, The Hague, Netherlands.

Korpus, R., and Falzarano, J.M., 1997, " Prediction of Viscous Ship Roll Damping by Unsteady Navier-Stokes Techniques," *J. of Offshore Mech. and Arctic Eng.*, vol. 119, no 2., pp. 108-113.

Sarpkaya, T, 1978, "Fluid Forces on Oscillating Cylinders," *J. Waterways, Port, Coastal Eng. Div. ASCE*, 104, pp 275-290.

Schulz, K., and Kallinderis, Y., 1997, "Unsteady Flow Structure Interaction for Incompressible Flows Using Hybrid Grids," AIAA.

Weems, K., and Korpus, R., et al., 1994, "Near-Field Flow Predictions for Ship Design," *Proceedings, 20<sup>th</sup> Symposium Naval*

*Hydrodynamics*, Santa Barbara, CA.

Yeung, R. W., and Vaidhyanathan, M., 1993, "Flow Past Oscillating Cylinders," *J. Offshore Mech. & Arctic Eng.*, v. 115, n. 4.